

# Diagnosing the Optically Thick/Thin Features Using the Intensity Ratio of Si IV Resonance Lines in Solar Flares

YI-AN ZHOU,<sup>1,2</sup> JIE HONG,<sup>1,2</sup> Y. LI,<sup>3</sup> AND M. D. DING<sup>1,2</sup>

<sup>1</sup>*School of Astronomy and Space Science, Nanjing University, Nanjing 210023, People's Republic of China*

<sup>2</sup>*Key Laboratory for Modern Astronomy and Astrophysics (Nanjing University), Ministry of Education, Nanjing 210023, People's Republic of China*

<sup>3</sup>*Key Laboratory of Dark Matter and Space Astronomy, Purple Mountain Observatory, Chinese Academy of Sciences, Nanjing 210033, People's Republic of China*

## ABSTRACT

In the optically thin regime, the intensity ratio of the two Si IV resonance lines (1394 and 1403 Å) are theoretically the same as the ratio of their oscillator strengths, which is exactly 2. Here, we study the ratio of the integrated intensity of the Si IV lines ( $R = \int I_{1394}(\lambda)d\lambda / \int I_{1403}(\lambda)d\lambda$ ) and the ratio of intensity at each wavelength point ( $r(\Delta\lambda) = I_{1394}(\Delta\lambda) / I_{1403}(\Delta\lambda)$ ) in two solar flares observed by the Interface Region Imaging Spectrograph. We find that at flare ribbons, the ratio  $R$  ranges from 1.8 to 2.3 and would generally decrease when the ribbons sweep across the slit position. Besides, the distribution of  $r(\Delta\lambda)$  shows a descending trend from the blue wing to the red wing. In loop cases, the Si IV line presents a wide profile with a central reversal. The ratio  $R$  deviates little from 2, but the ratio  $r(\Delta\lambda)$  can vary from 1.3 near the line center to greater than 2 in the line wings. Hence we conclude that in flare conditions, the ratio  $r(\Delta\lambda)$  varies across the line, due to the variation of the opacity at the line center and line wings. We notice that, although the ratio  $r(\Delta\lambda)$  could present a value which deviates from 2 as a result of the opacity effect near the line center, the ratio  $R$  is still close to 2. Therefore, caution should be taken when using the ratio of the integrated intensity of the Si IV lines to diagnose the opacity effect.

*Keywords:* line profiles — Sun: chromosphere — Sun: flares — Sun: UV radiation

## 1. INTRODUCTION

Solar flares can release a large amount of energy within a short period of time and affect all layers of the solar atmosphere including the chromosphere, the transition region (TR) and the corona (Fletcher et al. 2011). With a formation temperature of  $\sim 10^{4.8}$  K, the two cool Si IV resonance lines (1394 and 1403 Å) are excellent candidates to directly reveal the physical properties of the TR when small scale events occur, such as transition region explosive events (Innes et al. 1997; Teriaca et al. 2004; Huang et al. 2014, 2015, 2017; Chen et al. 2019; Reep et al. 2016; Warren et al. 2016), transient flows (McIntosh & De Pontieu 2009; Kleint et al. 2014), UV bursts (Peter et al. 2014; Hong et al. 2021), spicules (Tian et al. 2014b), microflares and nanoflares (Testa et al. 2014; Polito et al. 2018; Hannah et al. 2019). They have also been used in the study of solar flares, especially the properties of chro-

mospheric evaporation (Tian et al. 2014a; Li et al. 2015, 2017a,b, 2019; Brosius et al. 2016; Brosius & Inglis 2018) and chromospheric condensation (Zhang et al. 2016; Yu et al. 2020).

In the quiet Sun, the density of the TR and corona is low enough that the emitted Si IV photons can escape without distinct absorption, scattering or re-emission. Thus, these lines are usually regarded as optically thin. In the optically thin regime, the intensity ratio of these two lines, should be the same as the ratio of their oscillator strengths, which is exactly 2 (Mathioudakis et al. 1999). This theoretical value can also be obtained with the CHIANTI database (Dere et al. 1997; Del Zanna et al. 2021).

However, the intensity ratio can deviate from 2 in many observations. Yan et al. (2015) revealed self-absorption features of the Si IV line during a transient brightening event in an active region (AR). The line ratio of Si IV lines falls from  $\sim 2.0$  to  $\sim 1.7$  with the occurrence of the event and increases back to  $\sim 2.0$  near the end of the event. This self-absorption feature is in-

terpreted as a result of the overlying cool TR loops. Gontikakis & Vial (2018) also presented an observation that the intensity ratio between the Si IV 1394 and 1403 Å lines is greater than 2. This deviation is rendered to be the result of resonant scattering. Besides, Tripathi et al. (2020) made a detailed study of the spatial distribution and time evolution of the intensity ratio between the two Si IV lines in an emerging flux region. The intensity ratio varies a lot from the early phase to the late phase, with different values at the periphery and the core of an AR. The ratio in the quiet Sun regions is generally close to 2, and the difference of the ratio between the AR and the quiet Sun is usually ascribed to the opacity effect. In addition, Mulay & Fletcher (2021) found that the Si IV lines are mostly optically thin when the ratio is  $\sim 2$  at locations with strong H $_2$  emissions during the impulsive phase of a flare. However, at some locations of flare ribbons, the increased opacity causes the ratio to deviate from 2. Recently, a detailed theoretical calculation of the Si IV line profiles in flare models confirmed that due to the opacity effect, the intensity ratio of the Si IV lines at flare ribbons could vary from 1.8 to 2.3 (Kerr et al. 2019). Given the diverse results in observations and numerical simulations, it is still unclear if the Si IV lines are formed in optically thin or thick conditions in various solar activities, and how reliable it is to use the intensity ratio of the two lines to diagnose the opacity effects.

As for the intensity ratio of the Si IV lines, previous studies only focused on the ratio of the total intensity integrated over wavelength. However, in flare conditions the opacity should significantly vary from the Si IV line center to line wings. The photons at line wings can still escape freely from the solar surface while those at the line center might not (Kerr et al. 2019). In this case, it would be inappropriate to use the ratio of the integrated intensity as a diagnostics of opacity, since the opacity at the line center is quite different from that at line wings.

In this paper, we focus on the Si IV line profiles and investigate (1) the ratio of the integrated intensity of the Si IV lines ( $R = \int I_{1394}(\lambda)d\lambda / \int I_{1403}(\lambda)d\lambda$ ) and (2) the ratio of the intensity at each wavelength point relative to the line center of the Si IV lines ( $r(\Delta\lambda) = I_{1394}(\Delta\lambda) / I_{1403}(\Delta\lambda)$ ). The latter is based on the consideration that the two Si IV lines are formed at similar heights and thus their Doppler widths are almost the same in most cases. The rest of this paper is organized as follows. The observations from the Interface Region Imaging Spectrograph (IRIS; De Pontieu et al. (2014)) and data reduction are described in Section 2. The detailed results of the Si IV line profiles and line ratios

are shown in Section 3. Finally, Section 4 presents a summary and discussions.

## 2. OBSERVATIONS AND DATA REDUCTION

We study two solar flares (with M7.3 and C1.7 classes) observed with IRIS. The IRIS performed high-cadence sit-and-stare spectral observations with a slit width of 0."33 and a time cadence of 9.8 s for both flares. The spectral resolution of the FUV band covering the Si IV lines is  $\sim 0.025$  Å. An overview of these two flares with IRIS slit-jaw images (SJIs) as well as the spectra of the Si IV line at 1403 Å is displayed in Figure 1.

The M7.3 flare under study started at  $\sim 12:31$  UT, peaked at  $\sim 13:03$  UT and ended at  $\sim 13:20$  UT on 2014 April 18. The IRIS data cover the time period from  $\sim 12:33$  UT to  $\sim 17:18$  UT. In the impulsive phase of the flare, one can see clearly two flare ribbons (Figure 1(a), marked by R1 and R2, respectively) that lasted for minutes. The northern ribbon (R1) disappeared at  $\sim 13:20$  UT, while the southern ribbon (R2) disappeared earlier at  $\sim 12:57$  UT. We notice a hook structure of R2, which firstly appeared at  $\sim 12:43$  UT, reached the peak intensity at  $\sim 12:47$  UT (Figure 1(a)) and disappeared at  $\sim 12:50$  UT. The Si IV spectra at these flare ribbons display strong line and continuum emissions. There also appeared loop-like structures to the south of the flare ribbons which became more obvious at later time ( $\sim 13:02$  UT and  $\sim 13:16$  UT, Figure 1(b) and 1(c), marked by L1 and L2, respectively). The Si IV spectra at these loops display very wide line profiles. As for the C1.7 flare that Zhou et al. (2020) studied, it occurred in the active region NOAA 12673 near the solar limb. This flare started at  $\sim 06:51$  UT and peaked at  $\sim 06:56$  UT on 2017 September 9. Figure 1(d) illustrates the loop-like structures (L3) at  $\sim 06:56$  UT.

We then calculate the intensity ratio of the Si IV lines. As described above, we calculate both the ratio of wavelength-integrated intensity,  $R$ , and the ratio of intensity at each wavelength point,  $r(\Delta\lambda)$ . To improve the reliability, we first subtract the background continuum and the blended lines before calculations. The wavelength range for the calculations of both  $R$  and  $r(\Delta\lambda)$  is then specifically chosen to be where the intensity is three times larger than the standard deviation of the intensity fluctuations in the far wings. The data points where the line profiles are saturated or influenced by background cosmic rays are discarded.

## 3. RESULTS

The upper two panels of Figure 2 display space-time maps of the ratio  $R$  between the Si IV 1394 and 1403 Å lines and the integrated Si IV 1394 Å intensity at slit

positions for the M7.3 flare, while the lower two panels are for the C1.7 flare. The intensity contours in these panels show the evolutions of the flare ribbons and loops as described in Figure 1. We choose several positions in the flare ribbons and loops (labeled Rx-x and Lx-x) for further study, marked with black diamonds. The line profiles of these typical points are shown in Figures 3 and 4. We also choose five different slit positions and make horizontal cuts (labeled C1 to C5) in the space-time map to study the time evolution, marked with red dashed lines. The time evolution of the ratio  $R$  and line profiles at selected time instants are plotted in Figure 5.

### 3.1. Intensity ratio at flare ribbons

As shown in Figure 2, the ratio  $R$  is mostly close to 2 in the flare ribbons R1 and R2, but with deviations at some specific positions (Mulay & Fletcher 2021). The line profiles of Si IV 1394 and 1403 Å at the positions marked by black diamonds along flare ribbons are plotted in Figure 3 in blue and purple, respectively. The ratio  $r(\Delta\lambda)$  at each wavelength point is overplotted with error bars. In this M7.3 flare, it is seen that most of the Si IV lines present red asymmetries or red-shifted profiles in the ribbon area. For profiles at R1.1 and R1.2 (Figure 3(a)–(b)), though the ratio  $R$  deviates little from 2, the ratio  $r(\Delta\lambda)$  presents a tendency of decrease from the blue wing to the red wing, with a dip near the line center. The ratio  $r(\Delta\lambda)$  can be larger than 2 in the blue wing while smaller than 2 in the red wing. The profiles at R1.3 present double peaks (Figure 3(c)). At this position, the ratio  $R$  is  $\sim 1.8$ . The ratio  $r(\Delta\lambda)$  shows a similar distribution along wavelength to those at R1.1 and R1.2. We also find that the dip at R1.3 is much obvious than others. The variation of the ratio  $r(\Delta\lambda)$  along wavelength at R2 is generally similar to that at R1. However, the ratio  $R$  at R2.1 is much smaller than 2, while that at R2.2 and R2.3 is larger than 2.

### 3.2. Intensity ratio at loop cases

Figure 2 shows that the ratio  $R$  at the loop structures L1 and L2 are mostly close to 2, while at L3 it obviously deviates from 2.

Figure 4(a)–(d) presents the line profiles and intensity ratios of the Si IV 1394 and 1403 Å lines at the positions marked by black diamonds of the M7.3 flare. The most remarkable feature of these line profiles is an increased width with a central reversal. The central reversal has a depth of about half the peak intensity. Thus, we fit the line wings and the central reversal of the Si IV 1394 Å line with two Gaussian functions to derive the Doppler velocities corresponding to the plasma motions in the formation heights of line wings and line center, respectively. The central reversal is nearly static, while the

line wings shows a small red asymmetry. In Figure 4(c), it is seen that the the line emission at red wing is obviously enhanced, which may reflect the existence of some downward-moving plasma with large velocities.

In addition, the wavelength distribution of the ratio  $r(\Delta\lambda)$  is different from those in the flare ribbons. The ratio  $r(\Delta\lambda)$  here shows a symmetric distribution in the wings while the dip at line center is still very obvious.

Figure 4(e) and 4(f) illustrates the line profiles and intensity ratios of the Si IV 1394 and 1403 Å lines at L3.1 and L3.2 for the C1.7 flare. For the L3 loop, there appear notable continuum emissions at these positions (Figure 1), reflecting a possible overlapping of the flare loops with the flare ribbons along the line of sight. These line profiles show a very strong red peak, which was suggested to result from reconnection downflows (Zhou et al. 2020). The wavelength distribution of the ratio  $r(\Delta\lambda)$  looks similar to those of R1, with a general decrease from the blue wing to the red wing, and a dip at line center.

### 3.3. Time evolution of intensity ratio

The time evolution of the ratio  $R$  and the integrated intensity of Si IV 1394 Å at different slit positions as well as some selected Si IV 1394 Å line profiles are presented in Figure 5. It is seen that when the flare ribbons R1 and R2 sweep across the slit position, the integrated line intensity increases, while the ratio  $R$  decreases correspondingly, as shown for ribbon cases C1 to C3. The value of ratio  $R$  is generally below 2 at flare ribbons but over 2 at quiet Sun. However, we notice that the ratio  $R$  at C2 could quickly rise back to 2 after an initial fall. This is because at this time, the line profiles are very wide and show a strong peak in the red wing. The contribution from the line wing, which is closer to the optically thin scenario, thus increases the values of  $R$ . For loop cases C4 and C5, the intensity and ratio  $R$  do not vary much with time. The right panels of Figure 5 also display distinct dips at the center of Si IV 1394 Å line profiles when loop structures appear at the slit positions, but the ratio  $R$  is still close to 2.

## 4. CONCLUSIONS AND DISCUSSIONS

In this paper, we carry out an observational study about the intensity ratio between the Si IV 1394 and 1403 Å lines in two solar flares. We calculate the ratio of the integrated intensity,  $R$ , and the ratio of line intensity at each wavelength point,  $r(\Delta\lambda)$ , and explore their relation with the line opacity. Our observational results are summarized as follows:

- At the flare ribbons (R1 and R2), most of the Si IV line profiles show obvious redshifts or red asym-

metries with the ratio  $R$  ranging from 1.8 to 2.3. When the flare ribbons sweep across the slit position, the ratio  $R$  would generally decrease. The wavelength distribution of  $r(\Delta\lambda)$  shows a descending trend from the blue wing to the red wing, with a dip in the line center, in particular at R1.

- At the loop structures (L1 and L2), the Si IV line presents a wide profile with a central reversal. The line wings show a small redshift, while the central reversal is nearly static. The ratio  $R$  deviates little from 2.0, while the ratio  $r(\Delta\lambda)$  varies in a wide range, which is only 1.3 at the line center. Nevertheless, the distribution of  $r(\Delta\lambda)$  is nearly symmetric with wavelength.
- At some locations where the flare loops and flare ribbons possibly overlap (L3), the ratio  $r(\Delta\lambda)$  displays a similar wavelength distribution to that of R1.

The interesting result is that the ratio  $r(\Delta\lambda)$  can vary with wavelength in the line. This is reasonable given the fact that the opacity at the line center and line wings could be quite different under flare conditions. In fact, modeling of the Si IV lines at flare ribbons shows that for an intermediate flare, the opacity effect would not be negligible (Kerr et al. 2019). The opacity effect could explain the wavelength distribution of  $r(\Delta\lambda)$ , especially the central dip, at R1, R2 and L3. We notice that when the line profiles are significantly redshifted (L3\_2), the ratio  $r(\Delta\lambda)$  at the redshifted wing would be smaller than that in the line core. This suggests that the maximum opacity at each height always coincides with the local fluid velocity, as reported from previous flare simulations (Carlsson & Stein 1997; Kuridze et al. 2015; Kerr et al. 2019).

Under flare conditions, the values of  $R$  can also vary from case to case. For example, it can be close to 2 at R1\_1 and R1\_2, less than 2 at R1\_3 and R2\_1, and greater than 2 at R2\_2 and R2\_3. The opacity effect cannot explain the cases where  $R$  is greater than 2. One possible explanation for this result is the decreased contribution of the collisional excitations when resonant scattering is dominant, as proposed by Gontikakis & Vial (2018), who reported a negative relation between line ratio and electron density. In this work, we have estimated the electron density from the ratio of O IV 1401.2 and 1399.8 Å lines. We find that the electron density is around  $10^{10.3} \text{ cm}^{-3}$  in regions where  $R > 2$ , and is around  $10^{11.4} \text{ cm}^{-3}$  in regions where  $R < 2$ . These results agree with that of Gontikakis & Vial (2018). Rose et al. (2008) proposed that the specific geometry of the flaring plasma could also be a factor making the line ratio

greater than 2. Moreover, the formation heights of the two lines are slightly different. Comparatively, the 1394 Å line is formed slightly higher than the 1403 Å line. If the line source function has a larger gradient between the formation heights during the impulsive heating, it could also lead to a line ratio greater than 2. More observations and radiative hydrodynamic simulations are required to investigate the detailed physical mechanism that leads to these increased line ratios.

The central reversal in the Si IV line profiles in L1 and L2 looks very similar to the results of Yan et al. (2015), which was explained as an opacity effect. Correspondingly, the value of  $r(\Delta\lambda)$  can reach a central dip as low as 1.3, which is a typical feature of an optically thick case. However, the ratio  $R$  is still close to 2, as seen from the time evolution of this value (Figure 5). In these cases, the photons in the optically thick line core could be scattered to the wide line wings and easily escape since the line wings are still optically thin. Therefore, although the wavelength dependent line ratio  $r(\Delta\lambda)$  can significantly vary across the line, if the line ratio  $R$  of the integrated intensity is still equal to 2, it still implies that the whole line can be regarded as effectively optically thin.

Hence, we argue that the ratio of wavelength-integrated intensity cannot be served as a sole indicator of the opacity effect, especially when the line profiles are very wide. The line center and line wings could have different opacity effects, to say, the line center becomes optically thick while the line wings still keep optically thin in flare cases. Since the contribution of line wings is usually over that of the line center, the ratio of integrated intensity seems insensitive to the flare conditions. Therefore, it is highly required to use the ratio of intensity at each wavelength point to investigate the opacity effects of the Si IV lines, in addition to careful checking of the line profiles. We also note that, although the two Si IV lines are formed at close heights, they could still suffer from different Doppler shifts or asymmetries in the case that the flare-induced plasma velocity changes steeply (like chromospheric condensation). This can explain why the distribution of  $r(\Delta\lambda)$  is sometimes asymmetric, in particular at flare ribbons. How the asymmetry of  $r(\Delta\lambda)$  is related to flare dynamics deserves further investigation.

This work was supported by National Key R&D Program of China under grant 2021YFA1600504, and by NSFC under grants 11903020, 11733003, 12127901, 11873095, and 11961131002. Y.L. is supported by the CAS Pioneer Talents Program for Young Scientists and XDA15052200, XDA15320301, and XDA15320103.

IRIS is a NASA small explorer mission developed and operated by LMSAL with mission operations executed at the NASA Ames Research center and major con-

tributions to downlink communications funded by the Norwegian Space Center (NSC, Norway) through an ESA PRODEX contract.

## REFERENCES

- Brosius, J. W., Daw, A. N., & Inglis, A. R. 2016, *ApJ*, 830, 101.
- Brosius, J. W. & Inglis, A. R. 2018, *ApJ*, 867, 85.
- Carlsson, M. & Stein, R. F. 1997, *ApJ*, 481, 500.  
doi:10.1086/304043
- Chen, Y., Tian, H., Huang, Z., et al. 2019, *ApJ*, 873, 79.
- Dere, K. P., Landi, E., Mason, H. E., et al. 1997, *A&AS*, 125, 149.
- Del Zanna, G., Dere, K. P., Young, P. R., et al. 2021, *ApJ*, 909, 38
- De Pontieu, B., Title, A. M., Lemen, J. R., et al. 2014, *SoPh*, 289, 2733
- Fletcher, L., Dennis, B. R., Hudson, H. S., et al. 2011, *SSRv*, 159, 19
- Gontikakis, C. & Vial, J.-C. 2018, *A&A*, 619, A64.
- Hannah, I. G., Kleint, L., Krucker, S., et al. 2019, *ApJ*, 881, 109.
- Hong, J., Li, Y., Ding, M. D., et al. 2021, *ApJ*, 921, 50.
- Huang, Z., Madjarska, M. S., Xia, L., et al. 2014, *ApJ*, 797, 88.
- Huang, Z., Xia, L., Li, B., et al. 2015, *ApJ*, 810, 46.
- Huang, Z., Madjarska, M. S., Scullion, E. M., et al. 2017, *MNRAS*, 464, 1753.
- Innes, D. E., Brekke, P., Germerott, D., et al. 1997, *SoPh*, 175, 341.
- Kerr, G. S., Carlsson, M., Allred, J. C., et al. 2019, *ApJ*, 871, 23.
- Kleint, L., Antolin, P., Tian, H., et al. 2014, *ApJL*, 789, L42.
- Kuridze, D., Mathioudakis, M., Simões, P. J. A., et al. 2015, *ApJ*, 813, 125. doi:10.1088/0004-637X/813/2/125
- Li, D., Ning, Z. J., Huang, Y., et al. 2017a, *ApJ*, 849, 113
- Li, Y., Ding, M. D., Qiu, J., et al. 2015, *ApJ*, 811, 7
- Li, Y., Kelly, M., Ding, M. D., et al. 2017b, *ApJ*, 848, 118
- Li, Y., Ding, M. D., Hong, J., et al. 2019, *ApJ*, 879, 30
- Mathioudakis, M., McKenny, J., Keenan, F. P., et al. 1999, *A&A*, 351, L23
- McIntosh, S. W. & De Pontieu, B. 2009, *ApJ*, 707, 524.
- Mulay, S. M. & Fletcher, L. 2021, *MNRAS*, 504, 2842.
- Peter, H., Tian, H., Curdt, W., et al. 2014, *Science*, 346, 1255726.
- Polito, V., Testa, P., Allred, J., et al. 2018, *ApJ*, 856, 178.
- Reep, J. W., Warren, H. P., Crump, N. A., et al. 2016, *ApJ*, 827, 145.
- Rose, S. J., Matranga, M., Mathioudakis, M., et al. 2008, *A&A*, 483, 887. doi:10.1051/0004-6361:20079040
- Teriaca, L., Banerjee, D., Falchi, A., et al. 2004, *A&A*, 427, 1065.
- Testa, P., De Pontieu, B., Allred, J., et al. 2014, *Science*, 346, 1255724.
- Tian, H., Li, G., Reeves, K. K., et al. 2014a, *ApJL*, 797, L14.
- Tian, H., Kleint, L., Peter, H., et al. 2014b, *ApJL*, 790, L29.
- Tripathi, D., Nived, V. N., Isobe, H., et al. 2020, *ApJ*, 894, 128.
- Warren, H. P., Reep, J. W., Crump, N. A., et al. 2016, *ApJ*, 829, 35.
- Yan, L., Peter, H., He, J., et al. 2015, *ApJ*, 811, 48.
- Yu, K., Li, Y., Ding, M. D., et al. 2020, *ApJ*, 896, 154.
- Zhang, Q. M., Li, D., & Ning, Z. J. 2016, *ApJ*, 832, 65.
- Zhou, Y.-A., Li, Y., Ding, M. D., et al. 2020, *ApJ*, 904, 95.

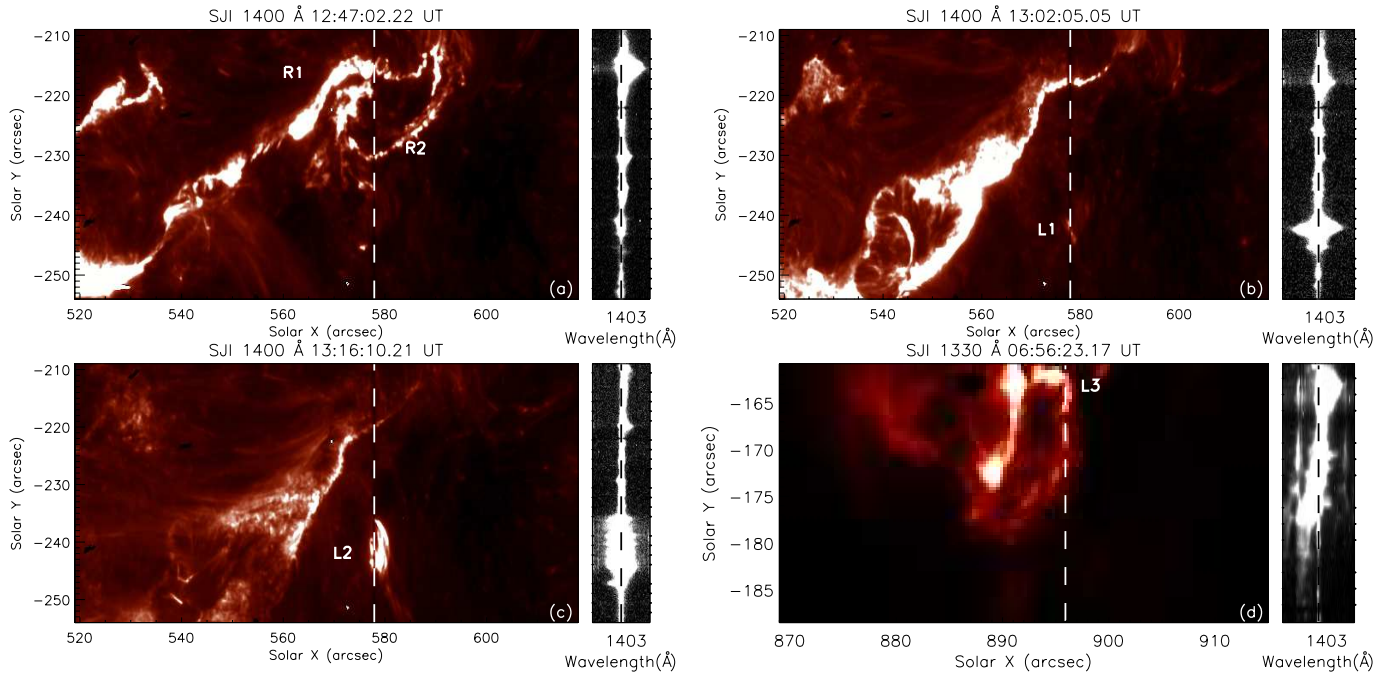


**Figure 1.** IRIS SJIs and Si IV 1403 Å spectra showing an overview of two solar flares. Panels (a)-(c) are for the M7.3 flare and (d) for the C1.7 flare. Flare ribbons (R1 and R2) and loops (L1-L3) are marked in each panel. White dashed lines in the SJIs mark the slit position, and black dashed lines in the spectra mark the line center of Si IV 1403 Å.

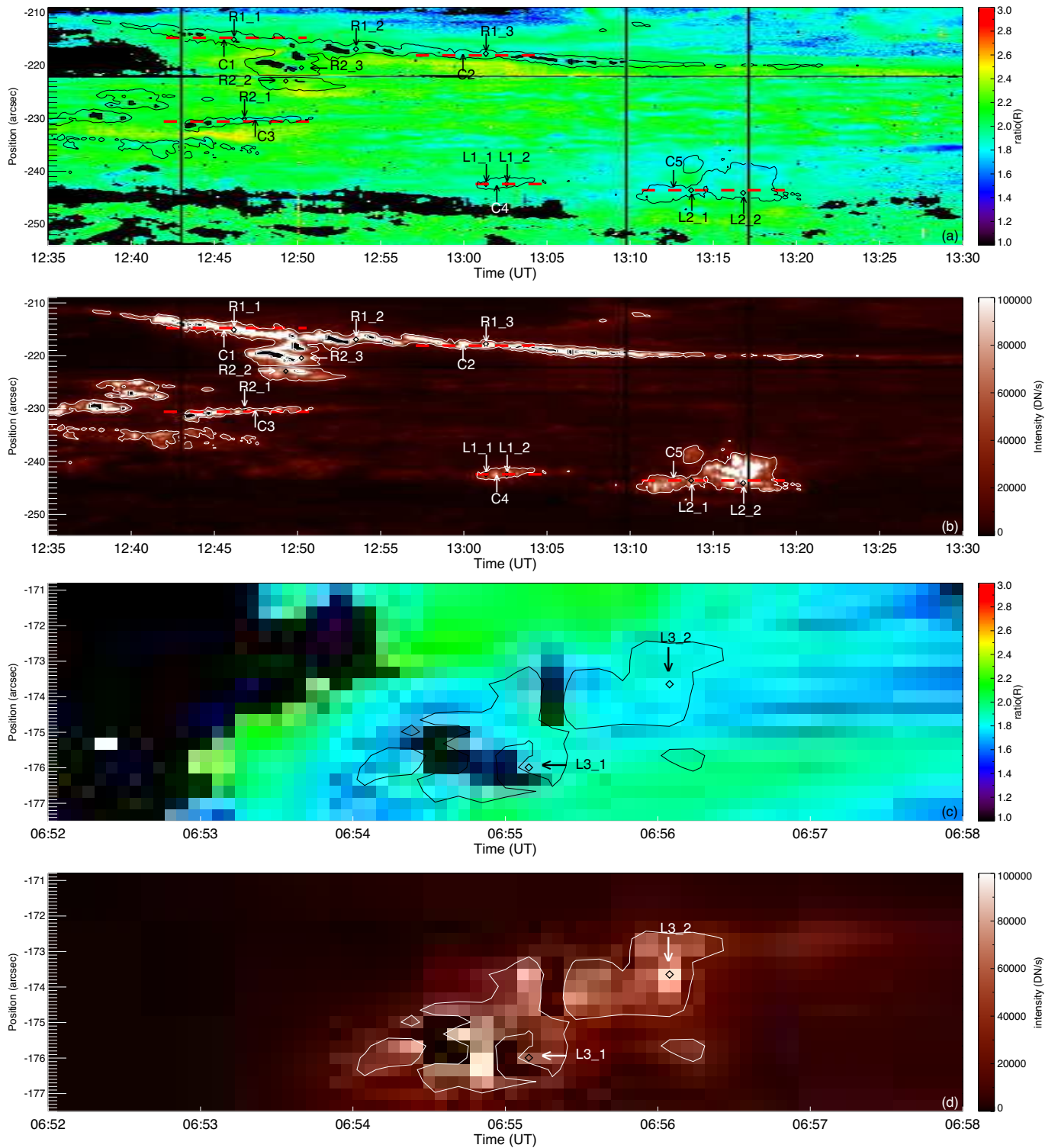


**Figure 2.** Panels (a)–(b) : The space-time maps of the intensity ratio  $R$  and the total intensity of the Si IV 1394 Å line for the M7.3 solar flare. Specific positions and horizontal cuts for further study are marked with black diamonds and red dashed lines, respectively. The contours indicate an intensity level of three times the average value of the total intensity of the Si IV 1394 Å line over the quiet region. The black area refers to positions where the spectra were overexposed or with a low signal-to-noise ratio, which are not used for analysis. Panels (c)–(d) : Same as panels (a)–(b), but for the C1.7 flare.

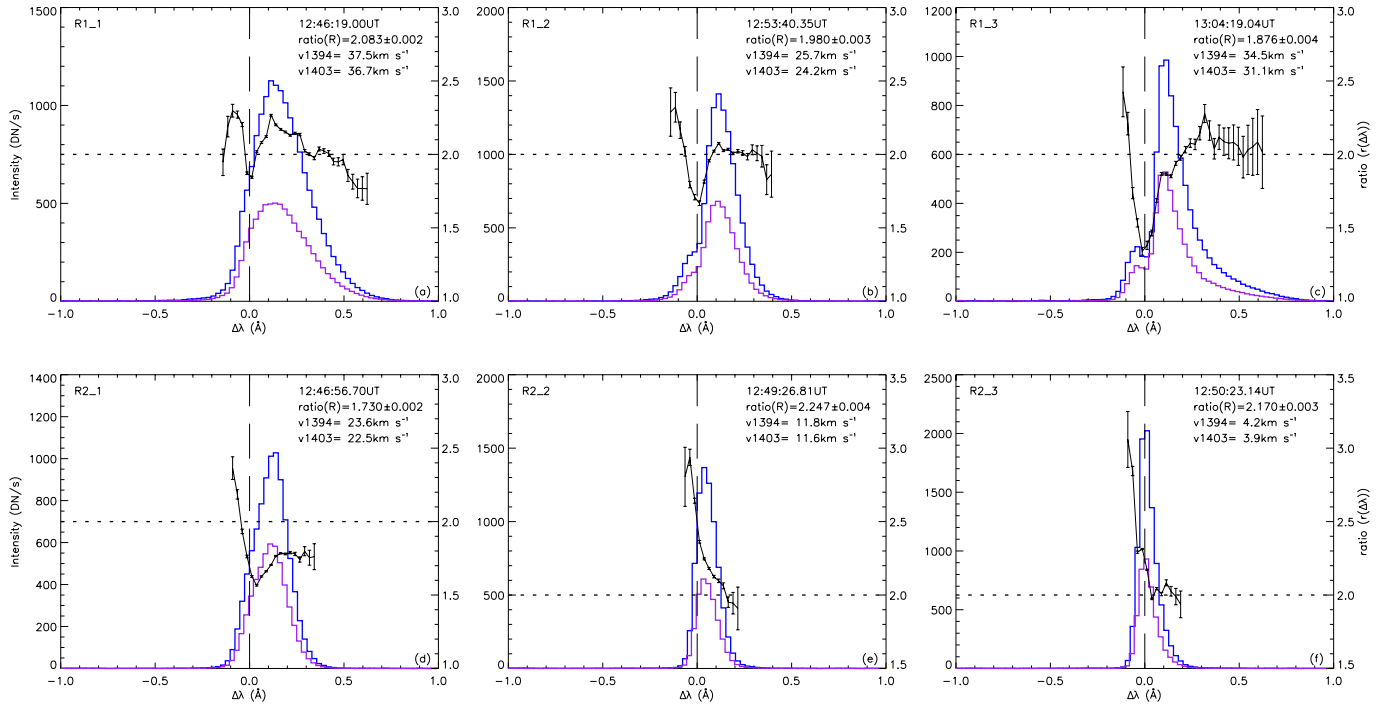


**Figure 3.** Line profiles of Si IV 1394 Å (blue) and 1403 Å (purple) at ribbon positions. In each panel, the dashed vertical line denotes the line center of the two Si IV lines, and the dashed horizontal line marks  $r(\Delta\lambda) = 2$ . The lines with error bars show the ratio ( $r(\Delta\lambda)$ ) between the two lines. The velocities in each panel are derived from the centroid of the Si IV line profiles.



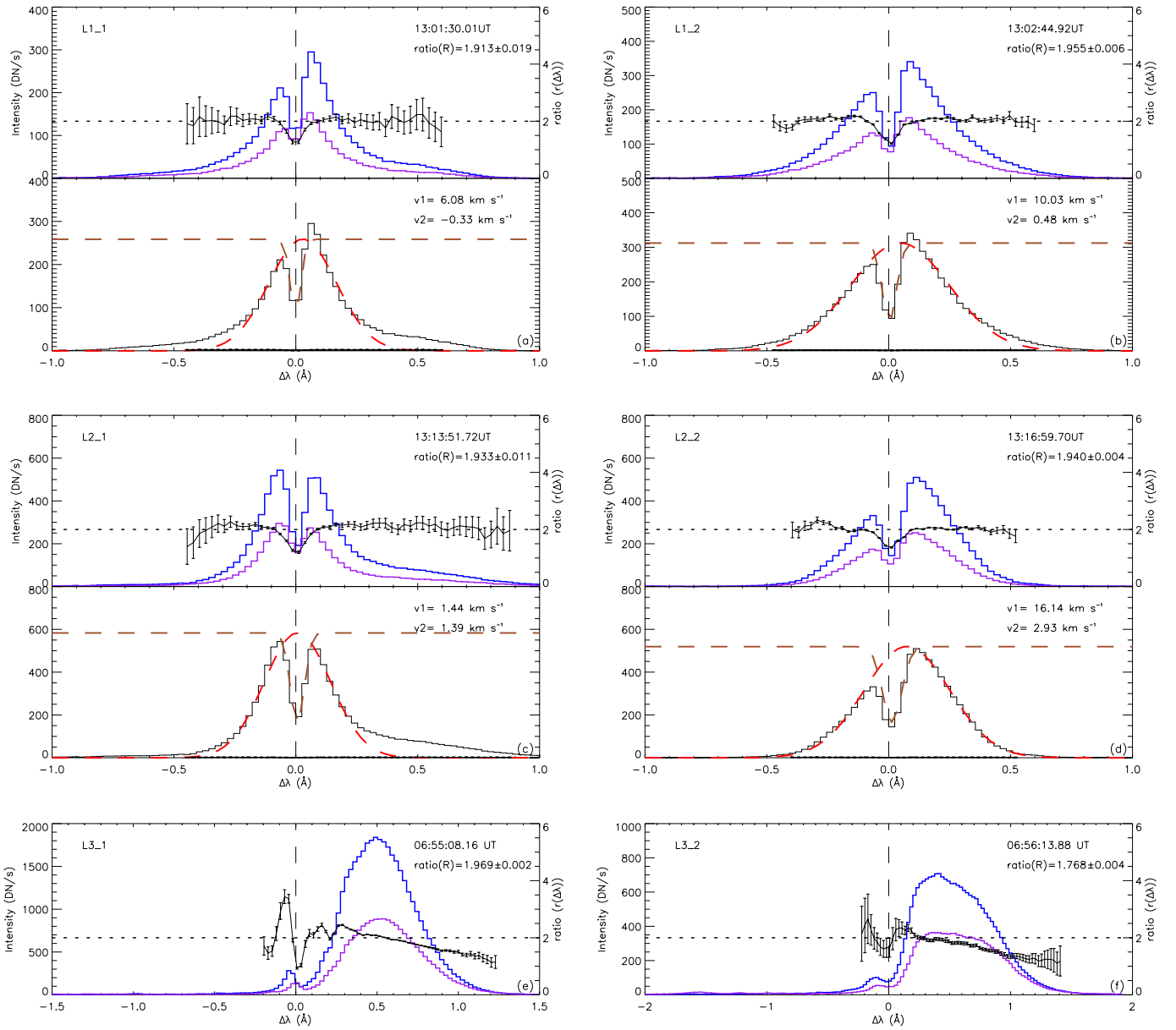


**Figure 4.** Same as Figure 3, but for loop positions. The two velocities  $v_1$  and  $v_2$  in panels (a)–(d) are derived from Gaussian fittings of the line wings and the central reversal, respectively.

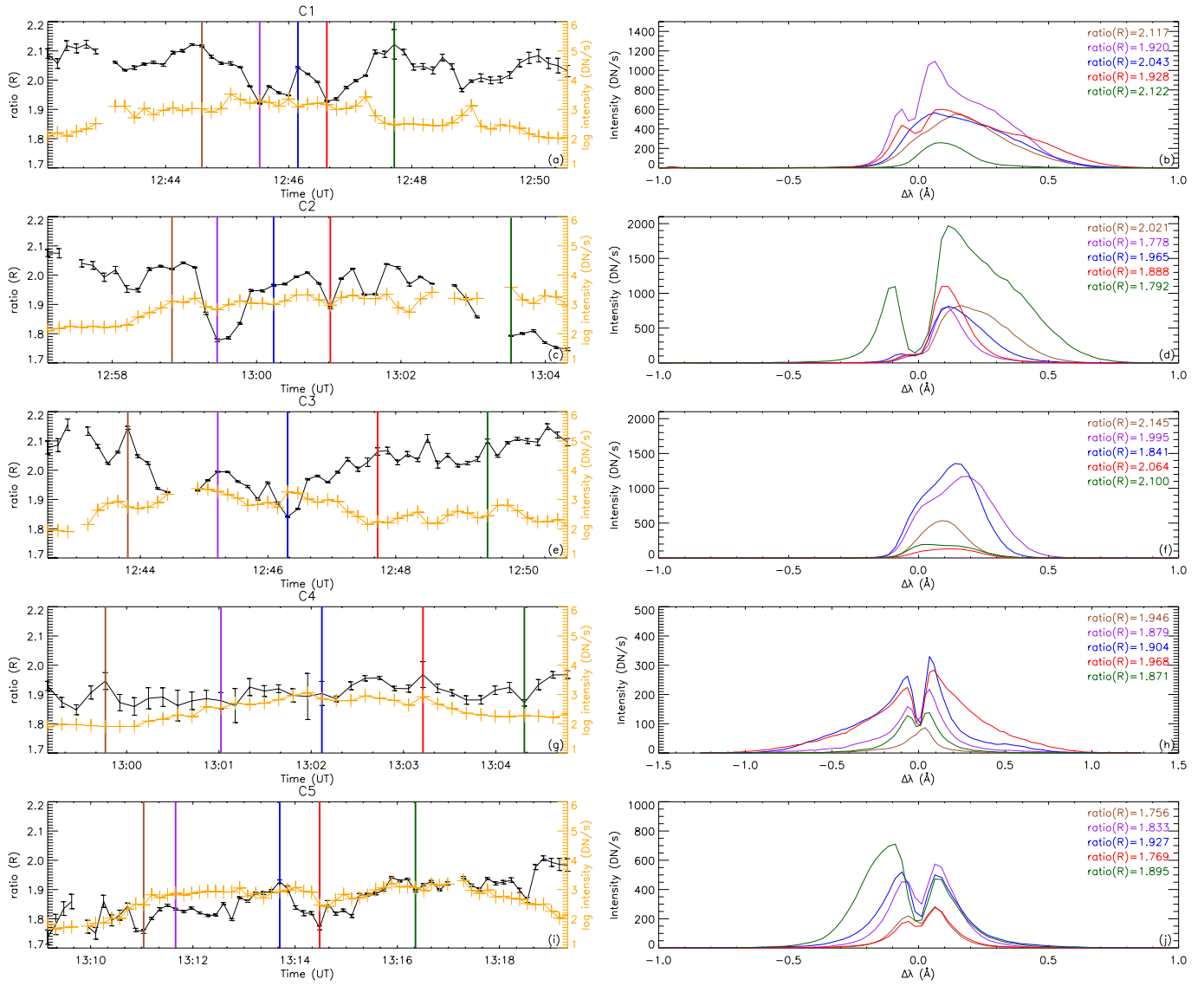


**Figure 5.** Left panels : Time evolution of the ratio  $R$  (black curves with error bars) and total intensity of the Si IV 1394 Å (plus signs) at different slit positions. Right panels: The selected Si IV 1394 Å line profiles at the slit positions shown in the left panels.